Diffusion Monte Carlo Approaches for Evaluating Rotationally Excited States of Symmetric Top Molecules: Application to H_3O^+ and D_3O^+†

Andrew S. Petit and Anne B. McCoy*

Department of Chemistry, The Ohio State University, Columbus, Ohio 43210

Received: May 30, 2009; Revised Manuscript Received: July 15, 2009

An approach is described for evaluating energies and wave functions for rotationally excited states of symmetric top molecules using diffusion Monte Carlo methods. The approach is based on the fact that, for many systems, the rotation/vibration Hamiltonian can be modeled by terms that depend on the vibrational coordinates and powers of the components of the rotational angular momentum vector, $\vec{J}$. In the case of symmetric top molecules with $M = 0$, the rotational part of the wave function is given by the tesseral harmonics. We construct rotationally excited states within the diffusion Monte Carlo approach by imposing nodal surfaces that are obtained from the roots of the tesseral harmonics. Results are presented for H_3O^+ and D_3O^+ with $J \leq 10$. Where comparisons to previous calculations can be made, the agreement is excellent.

1. Introduction

High resolution, rotationally resolved, spectra provide among the most sensitive probes of molecular structure, rotation/vibration couplings, and intramolecular vibrational energy redistribution.[1] Interestingly, in many systems, including ones that exhibit large amplitude vibrational motions, the rotational band contours are described well by the model Hamiltonian,

$$\hat{H}_{\text{rot}} = A_v \hat{J}_A^{\,2} + B_v \hat{J}_B^{\,2} + C_v \hat{J}_C^{\,2} \tag{1}$$

plus higher order terms. Here the values of the rotational constants depend on the specific vibrational level. In some systems, like CH_3OH, in which there is a large amplitude internal rotor, additional terms are needed but the rotational energies can still be modeled by simple analytical functions of the rotational quantum numbers.[2,3] While this observation is at first surprising, it makes modeling observed rotational data relatively straightforward for many molecular systems.

The observation that eq 1 captures the rotational band contour implies that one should be able to calculate the corresponding vibrationally averaged rotational constants for each vibrational state and use them to model the spectrum. One might also be tempted to conclude that these rotational constants are given by expectation values of the diagonal elements of the inverse moment of inertia tensor.

The situation is not as simple as is implied by the form of eq 1. The reason is that eq 1 results from applying second-order perturbation theory to the rotation−vibration Hamiltonian. As van Vleck pointed out,[4] the coefficients in this expression contain contributions from both the vibrationally averaged rotational constants and the Coriolis coupling terms, which are introduced as first-order corrections to a zero-order rigid rotor/harmonic oscillator Hamiltonian. In most systems, these terms are small and are treated well by perturbation theory.

While the energies obtained either from converged variational calculations that employ the full rotation-vibration Hamiltonian or from second-order perturbation theory[5] will be independent of how the body-fixed axis system is defined, the contribution to A_v, B_v, and C_v from Coriolis terms in the Hamiltonian will depend sensitively on the choice of embedding of the body-fixed axis system.[6−8] A common choice is an Eckart frame,[9,10] which has two advantages. First, it captures the rotational symmetry of the molecule and retains this symmetry when the molecule is in a totally symmetric vibrational state. It also minimizes the size of the Coriolis coupling terms in the rotation-vibration Hamiltonian.[9,11] Unfortunately, no embedding can completely remove these terms.[12]

Based on the above, one is left to conclude that the values of $\langle A \rangle_v$, $\langle B \rangle_v$, and $\langle C \rangle_v$ will depend on the choice of embedding. The Eckart frame is arguably the best choice to work with. Even when it is used, assigning the rotation−vibration spectrum using the vibrationally averaged rotational constants can be complicated. This will be particularly severe when the system of interest contains one or more coordinates that display large amplitude vibrational motions that result in large Coriolis couplings.[2]

To investigate rotation−vibration couplings, we pursue a slightly different approach, focusing on the evaluation of rotationally excited states and their energies using diffusion Monte Carlo (DMC) simulations.[13,14] This approach has been applied successfully to studies of the ground and excited vibrational states of molecules and molecular ions that undergo large amplitude vibrational motions.[7,15−19] It has also been applied to studies of rotationally excited states of molecules embedded in quantum clusters.[20,21] These investigations have fallen into two classes. The first, employed by Roy, Whaley, and Singer, follows the work of Ceperley and Bernu[22] and uses correlation function approaches to obtain excited state energies using a trial function with the appropriate symmetries. This approach can yield accurate energies but does not provide the wave function. A second approach, which we have had good success with,[18,23] involves using a fixed-node treatment in which the nodes that define the excited state are predetermined and the DMC method is used to evaluate the lowest energy state with nodes in the prescribed locations. The predetermination of the nodal structure introduces a more severe approximation

† Part of the "Russell M. Pitzer Festschrift".

* Corresponding author. E-mail: mccoy@chemistry.ohio-state.edu.

10.1021/jp905098k CCC: $40.75
Published on Web 08/13/2009

to the excited states than the correlation function approaches. On the other hand, this treatment allows us to generate wave functions.

In this work, we explore the effectiveness of fixed-node DMC for evaluating rotationally excited states of molecules that undergo one or more large amplitude vibrations. Specifically, drawing from the effectiveness of eq 1 in describing rotationally excited states and the fact that, for symmetric top molecules, the Wigner rotation matrices are eigenstates of $\hat{H}_{rot}$, we perform fixed-node calculations on rotationally excited states of H_3O^+ and D_3O^+ for all states with $J = 0$, 1, and 2, as well as the states $|J,0,0\rangle$ and $|J,J,0\rangle_\pm$ with $J = 6$ and 10. We chose to focus on H_3O^+ and D_3O^+ for three reasons. First, they have a low barrier to inversion (700 cm^{-1}) and hence undergo large amplitude, zero-point motion along the umbrella inversion coordinate. Second, two high-quality potential energy surfaces (PESs) for H_3O^+ have been reported by Bowman and co-workers[24] and by Halonen and co-workers.[25] Finally, Bowman and co-workers have calculated the energies of the $J = 0$ and $J = 1$ states of H_3O^+ and D_3O^+ using their potential surface, providing energies against which we can benchmark our DMC calculations.[24]

The primary goal of this work is to investigate the quality of the fixed-node treatment for generating rotationally excited states of H_3O^+ and D_3O^+. We are also interested to see if the DMC simulations are sensitive to the expected couplings between rotational motion, particularly about the symmetry axis, and the inversion coordinate. This should be seen through the dependence of the vibrational wave function on the rotational quantum numbers. The longer term goals of this work are to investigate molecules like CH_5^+ that undergo much larger amplitude motions and to study asymmetric top molecules with $J \geq 2$.

2. Theory

2.1. General Diffusion Monte Carlo Methodology. The diffusion Monte Carlo (DMC) methodology has been discussed elsewhere, and here we provide a general overview.[15,26,27] The impetus for the method is the observation that when expressed in terms of the imaginary time variable, $\tau = it/\hbar$, the time-dependent Schrödinger equation becomes formally identical to the classical diffusion equation, making it amenable to solution via simulation.[13,14] We will develop the details of this simulation by appealing to the general expression for the imaginary time evolution of a state vector,

$$|\Psi(\tau + \delta\tau)\rangle \simeq e^{-(\hat{V}-E_{ref})\delta\tau} e^{-\hat{T}\delta\tau} |\Psi(\tau)\rangle \quad (2)$$

within the standard split-operator approximation and with an added reference energy, E_{ref}.[28] To turn this into a recipe for a simulation, we choose a basis consisting of an ensemble of independently evolving δ-functions, or walkers, that are distributed throughout the $3N$-dimensional configuration space of the molecule of interest. In this basis, the action of the kinetic energy contribution to the propagator can be shown to be reproduced by the diffusion of the walkers, with each walker undergoing a random displacement in each Cartesian coordinate obtained from a Gaussian distribution of width

$$\sigma_i = \sqrt{\frac{\delta\tau}{m_i}} \quad (3)$$

where m_i is the mass associated with the ith Cartesian coordinate. Similarly, the action of the potential energy contribution to the propagator corresponds to the addition or deletion of walkers from the ensemble. Specifically, if the ith walker is at $\vec{x}_i$, then the integer contribution to $e^{-(V(\vec{x}_i)-E_{ref})\delta\tau}$ provides the number of walkers that are added to the ensemble at $\vec{x}_i$. The remainder provides the probability that the original walker remains in the ensemble.

The simulation outlined above provides a means to probe the ground state energy and wave function of the system. To see this, note that an arbitrary state vector, expanded in terms of the eigenstates of the system's Hamiltonian and with a global phase factor of $e^{itE_{ref}/\hbar}$, is written in terms of τ as

$$|\Psi(\tau)\rangle = \sum_n c_n e^{-(E_n-E_{ref})\tau} |\phi_n\rangle \quad (4)$$

From this, we see that if E_{ref} is set equal to E_0, then the contributions from the excited states to the above expansion decay exponentially with τ and $|\Psi(\tau)\rangle$ converges to the system's ground state. Because the ground state energy is not known a priori, one varies E_{ref} throughout the simulation via

$$E_{ref}(\tau) = \langle V(\tau)\rangle - \alpha\frac{N(\tau) - N(0)}{N(0)} \quad (5)$$

where $\langle V(\tau)\rangle$ is the instantaneous average potential energy of the walkers, $N(\tau)$ is the instantaneous population of walkers, and α is a simulation parameter.[13] As the simulation proceeds, E_{ref} rapidly converges to the ground state energy of the system, fluctuating around it once equilibrium is established. Likewise, once the simulation reaches equilibrium, the distribution of walkers fluctuates about the system's ground state wave function.

Descendent weighting is used throughout this study to obtain expectation values and probability distributions.[15,26] Briefly, one obtains the expectation value of the multiplicative operator $\hat{A}$ via

$$\langle A\rangle = \frac{\sum_i A(\vec{x}_i) w_i}{\sum_i w_i} \quad (6)$$

where the sums are over some instantaneous distribution of walkers. The weights, w_i, are obtained by counting the number of surviving descendants of the ith walker, including the walker itself, after a predetermined number of time steps, N_{step}. In essence, the instantaneous distribution of walkers provides one copy of the ground state wave function while the weights effectively provide a second; a walker in a low-energy region of the potential, where we would expect a relatively large amplitude of the wave function, will tend to have a larger number of surviving descendants than a walker in a high-energy region.

2.2. Applying the DMC Method to Rotationally Excited States. Although the DMC method naturally samples the ground state, we use the fixed-node methodology to study rotationally excited states.[29,30] Fixed-node DMC is based on the observation that a wave function goes to zero with finite slope in the vicinity of either a node or an infinite potential barrier. Moreover, the nodal surfaces in an excited state wave function divide all of configuration space into a series of nodal regions, within each

of which the wave function does not change sign. On the basis of these observations, we perform a DMC simulation using a modified potential consisting of the sum of the system's original PES with an infinite potential barrier throughout all of configuration space except a given nodal region of the excited state of interest. Because the amplitude of a wave function is necessarily zero in regions where the potential is infinite, the effect of the above modification to the potential is to confine the walkers to a single nodal region, with any walker that attempts to diffuse out of this region being removed from the simulation. If the exact nodal surfaces for the excited state of interest are used in the fixed-node calculation, then as the DMC simulation proceeds, E_{ref} will converge to the energy of this excited state, while the distribution of walkers will converge, to within a multiplicative constant, to the portion of the excited state wave function within that nodal region.

The nodal surfaces used in this study are defined within the confines of two assumptions. First we assume that rotational and vibrational motion are sufficiently uncoupled that we can express the nodal surfaces of rotationally excited states in terms of only the rotational coordinates $\{\theta, \chi, \phi\}$. Second, we assume that the Wigner rotation matrices provide a reasonable description of the projection of the system's true state vector onto the rotational coordinates. In particular, we assume that, to within a phase factor,

$$\begin{aligned}\langle\theta,\chi,\phi|J,K,M=0\rangle &= \frac{T_J^{K,\pm}(\theta,\chi)}{\sqrt{2\pi}} \\ &= \frac{Y_J^K(\theta,\chi) \pm (-1)^K Y_J^{-K}(\theta,\chi)}{\sqrt{4\pi(1+\delta_{K,0})}} \end{aligned} \tag{7}$$

and use the roots of the tesseral harmonics, $T_J^{K,\pm}(\theta,\chi)$, to define the nodal surfaces used in the DMC simulation of the states $|J,K,0\rangle_{\pm}$.[31] Specifically, because $T_J^{K,\pm}(\theta,\chi)$ can be factored as

$$T_J^{K,\pm}(\theta,\chi) = \Theta_{J,K}(\theta)\, X_{K_\pm}(\chi) \tag{8}$$

these nodal surfaces take the form of $\theta = \theta_{\mathrm{node}}$ or $\chi = \chi_{\mathrm{node}}$. Although the verity of the chosen functional forms of a given set of nodal surfaces cannot be straightforwardly assessed, we can systematically consider the quality of a specific set of nodal surfaces by comparing the results of DMC simulations performed in each of the nodal regions. If the average energies obtained in these simulations agree, to within the statistics, then we can be confident that we have found the optimal set of nodal surfaces associated with our chosen functional forms. It should be noted that the above treatment of the rotational component of the wave function will only be appropriate for molecules that can be classified as spherical tops, symmetric tops or asymmetric tops with $J \leq 1$ as well as a limited number of higher J states of asymmetric top molecules.

Given their importance in this study, we now consider how the rotational coordinates are obtained. Recall that for a rigid body, $\{\theta, \chi, \phi\}$ are the Euler angles that transform a set of space axes, whose origin is fixed at the center of mass, into the chosen body-fixed axis system. Moreover, recall that the body-fixed axes are designed to, in their own evolution, capture all of the system's rotational motion; i.e., a rigid body is stationary inside a body-fixed axis frame. However, we are interested in probing the rotationally excited states of molecules that undergo large amplitude, zero-point vibrational motion and therefore are not well-described by the rigid rotor model. For these systems, we employ an Eckart embedding, the evolution of which captures as much of the molecule's rotational motion as possible, in the process maximally uncoupling rotation and vibration.[9,10] Therefore, we obtain $\{\theta, \chi, \phi\}$ from the unitary matrix that transforms a given molecular geometry from the space-fixed to the Eckart frame. Note that the partial uncoupling of rotation and vibration inside the Eckart frame provides a partial justification for the first assumption underlying our choice of nodal surfaces.

The complete wave function for an excited state can be constructed by splicing together all of the pieces obtained from a series of fixed-node DMC simulations performed in the various nodal regions. The challenge here lies in the fact that, generally, each section of the wave function has a different relative amplitude, which is not known a priori. Focusing on states with $M = 0$, we assume that the tesseral harmonics provide a reasonable approximation to the true rotational component of the wave function and use them to develop the weights that are used when splicing all of the segments together. For the $|K| = J$ states, as well as for any nodes in χ, this implies that we weight all nodal regions equally. When $|K| \neq J$, on the other hand, we use the following expression as the weight for the nodal region defined by $\theta_i < \theta < \theta_{i+1}$.

$$w_i = \int_0^{2\pi} \int_{\theta_i}^{\theta_{i+1}} |T_J^{K,\pm}(\theta,\chi)|^2 \sin(\theta)\, \mathrm{d}\theta\, \mathrm{d}\chi \tag{9}$$

Note that, although we have chosen to focus on states with $M = 0$ in this study, preliminary calculations of the states with $J = 1$ and $|M| = 1$ have been performed and the obtained energies are identical, within the statistics, to the analogous $M = 0$ states.

Finally, because we use a finite time step, a correction is implemented to account for the possibility of a walker crossing and then recrossing a nodal surface within a single time step. The general expression for the probability that a walker should be removed from the simulation because it has crossed and then recrossed a given nodal surface during the time step from τ to $\tau + \delta\tau$ is

$$P_{\mathrm{recross}} = \exp\left[-\frac{m_{\mathrm{eff}} d(\tau)\, d(\tau+\delta\tau)}{\delta\tau}\right] \tag{10}$$

where m_{eff} is the effective mass associated with the nodal coordinate and $d(\tau)$ is the distance from the nodal surface at imaginary time τ.[14] As the nodal surfaces used in this study take the form of either $\theta = \theta_{\mathrm{node}}$ or $\chi = \chi_{\mathrm{node}}$, the appropriate distances to use in eq 10 will be $d(\tau) = \theta(\tau) - \theta_{\mathrm{node}}$ or $d(\tau) = \chi(\tau) - \chi_{\mathrm{node}}$, where all angles are measured in radians. For a symmetric rotor like H_3O^+, the appropriate m_{eff} for a node in θ is taken to be

$$m_{\mathrm{eff},\theta} = \sqrt{\left[\frac{I_{AA}(\tau)+I_{BB}(\tau)}{2}\right]\left[\frac{I_{AA}(\tau+\delta\tau)+I_{BB}(\tau+\delta\tau)}{2}\right]} \tag{11}$$

while for a node in χ we use

$$m_{\mathrm{eff},\chi} = \sqrt{I_{CC}(\tau)\, I_{CC}(\tau+\delta\tau)} \tag{12}$$

Here, for example, $I_{CC}(\tau)$ is the diagonal element of the moment of inertia tensor, **I**, associated with the symmetry axis of the system as calculated in the Eckart frame at imaginary time τ.

While the use of the elements of **I** in the expressions for m_{eff} is readily understood from both unit analysis and the fact that we are working with rotational motion, the specific forms of $m_{\text{eff},\theta}$ and $m_{\text{eff},\chi}$ demand further explanation. We begin by noting that the $|J,0,0\rangle$ states possess rotational motion about some combination of the *A* and *B* axes while their projection onto the rotational coordinates only contains nodes in θ. Similarly, the $|J,J,0\rangle_{\pm}$ states have the maximum possible component of angular momentum along the symmetry axis while their corresponding rotational wave functions only contain nodes in χ. It is therefore reasonable, at least for $|J,0,0\rangle$ and $|J,J,0\rangle_{\pm}$, that $m_{\text{eff},\theta}$ involves the average of I_{AA} and I_{BB} while $m_{\text{eff},\chi}$ involves I_{CC}. From the series of tesseral harmonics associated with a given value of *J*, we see that there are *K* nodes in χ. This observation, along with the orthogonality of the nodal surfaces in θ and χ, allows us to generalize our expressions for $m_{\text{eff},\theta}$ and $m_{\text{eff},\chi}$ to rotationally excited states with $0 < |K| < J$. Finally, because **I** depends on the instantaneous molecular geometry of the system, it is not constant, and as a result, we use the geometric mean of the matrix elements before and after the time step.

2.3. Computational Details. The global PES of H_3O^+ developed by Bowman and co-workers was used throughout this study.[24] After some initial parameter optimization, we selected a time step, $\delta\tau$, of 1 atomic unit, an initial population of 20 000 walkers, $N(0) = 20\,000$, and an α value of 0.5 hartree. The ground state calculations began with a 20 000 and 30 000 time step equilibration period for H_3O^+ and D_3O^+, respectively. The ensemble for D_3O^+ required a longer time to equilibrate due to its larger mass and therefore smaller displacements at each time step.

The excited state simulations for both H_3O^+ and D_3O^+ were initiated from distributions of walkers that were obtained from ground state simulations of H_3O^+ that contained as many as 100 000 walkers and had been run for 5000 time steps. A large population of walkers was used for this purpose to ensure that every nodal region contained at least 450 walkers at the start of the simulation. This also accelerated the rate of equilibration of the excited state simulations. Note that, despite starting with as many as 25 000 walkers, the excited state simulations always used $N(0) = 20\,000$ in eq 5. The simulations were run for a 20 000 time step equilibration period before gathering information about the excited state energy and wave function. This was found to yield converged energies for the excited states of both species.

After the equilibration period, we began the 62 500 time step production portion of the simulation, during which $E_{\text{ref}}(\tau)$ was collected and averaged. After the first 25 000 time steps of this production period, copies of the instantaneous distribution of walkers were saved every 2500 time steps. The 2500 time step delay was chosen to ensure the statistical independence of the wave functions. For each of these distributions, we also obtained the number of surviving descendants of each walker after 250 time steps, i.e., $N_{\text{step}} = 250$. Finally, 5 statistically independent DMC simulations were performed in each nodal region of the excited states while 10 simulations of the ground state were performed.

3. Results

3.1. Analysis of the Energies. The energies of the ground and $J = 1$ rotationally excited states of H_3O^+ and D_3O^+ are reported in Table 1. While our method cleanly resolves the rotational states of H_3O^+, the roughly 2 cm^{-1} splitting between the $|1,0,0\rangle$ and $|1,1,0\rangle_{\pm}$ states of D_3O^+ is too small for us to resolve with 99% confidence intervals. For both species, the DMC energies of the degenerate $|1,1,0\rangle_{\pm}$ states are identical within the error bars.

TABLE 1: Comparison between DMC and RVIB4[24] Energies (cm^{-1}) for $J = 0$ and $J = 1$ States

	H_3O^+		D_3O^+	
state	DMC[a,b]	RVIB4[b]	DMC[a,b]	RVIB4[b]
$\|0,0,0\rangle$	7452.51 ± 1.98	7451	5474.62 ± 1.70	5474
$\|1,1,0\rangle_+$	16.75 ± 3.27	17.4	9.13 ± 2.42	8.9
$\|1,1,0\rangle_-$	17.61 ± 2.78	17.4	9.36 ± 2.80	8.9
$\|1,0,0\rangle$	23.12 ± 2.60	22.3	11.98 ± 2.21	11.3

[a] Reported error bars are 99% confidence intervals. [b] Excited state energies reported relative to ground state values.

Table 1 also compares our DMC results to the energies obtained by Bowman and co-workers using RVIB4.[24] Because the same PES was used in both studies, Table 1 provides a direct comparison between the two methods for solving the nuclear Schrödinger equation. Referring to the table, one sees at once that the agreement between the two methods is excellent, with all of the differences lying within our 99% confidence intervals, and that the energies obtained from our DMC simulations are only 1 cm^{-1} higher than those reported by Huang et al.

In our initial studies of the above states of H_3O^+, we used the C_{3v} equilibrium structure as the reference geometry for the determination of the Eckart frame. This led to a large number of improper rotation matrices linking the space-fixed and Eckart frames. In addition, the energies obtained from these DMC simulations were in excellent agreement with the sum of the rotational excitation energy and the tunneling splitting reported by Huang et al.[24] This result indicates that, due to our choice of reference geometry, nodal surfaces were placed along both the rotational and inversion coordinates. It seems that by choosing a reference geometry that is localized in one of the two equivalent wells of the umbrella inversion coordinate, we inadvertently probed the manifold of rotationally excited states associated with the upper state of the tunneling doublet. Changing the reference geometry to the D_{3h} saddle point removed any bias of one well over the other in the simulation. By removing the node in the inversion coordinate, we completely eliminated the improper rotation matrices.

Table 2 provides a summary of the results of our DMC simulations, along with a comparison with experiment,[32,33] for the $J = 1$ and $J = 2$ states of both H_3O^+ and D_3O^+. Focusing first on just the DMC data, we note that our method continues to resolve the splitting between all of the rotational levels of H_3O^+ but is unable to differentiate between some of the more closely spaced energy levels of D_3O^+ within the statistics of the simulation. The degeneracy of the $|J,K,0\rangle_{\pm}$ pairs continues to be reproduced by our method, with the energies of all such pairs showing no statistically significant difference at the 1% level. For both species, the agreement between theory and experiment is excellent. Indeed, only the $|2,2,0\rangle_+$ state of D_3O^+ shows a statistically significant difference between the calculated and experimental energies, E_{calc} and E_{expt}, at the 1% level. Finally, it is worth noting that the DMC simulations nearly exclusively predict energies that are larger than experiment. We will return to this point in section 4.

In addition to experiment, Table 2 also provides the results of a rigid rotor fit to the DMC data of the states with $J \leq 2$. Specifically, we used the following energy level expression for the fit

$$E_{\mathrm{fit}}(J,K) = BJ(J+1) - (B-C)K^2 + E_0 \qquad (13)$$

where B, C, and E_0 are fit parameters. These parameters, along with those of a similar fit using all of the states considered in this study, are listed in Table 3. Note that the error bars for our calculated energies were not taken into account during the fitting. Importantly, we see that the DMC energies of the first nine rotationally excited states of both H_3O^+ and D_3O^+ are well described by the simple rigid rotor energy level expression given above. For comparison, we also report the vibrationally averaged rotational constants, which are obtained from the ground state wave function using approaches described elsewhere.[26] As anticipated above, there are deviations between the calculated and fit rotational constants that are larger than the uncertainties of either calculation. Further when we use the vibrationally averaged rotational constants to predict the excited state energies, there are generally larger deviations from the DMC energies than the $E_{\mathrm{calc}} - E_{\mathrm{fit}}$ values reported in Tables 2 and 4.

The energies of the selected $J = 6$ and $J = 10$ states considered in this study are reported and compared to experiment in Table 4. One should first note that our DMC simulations continue to reproduce the degeneracy of the $|J,J,0\rangle_{\pm}$ states, an important check of the method's internal consistency. However, statistically significant differences between theory and experiment, $E_{\mathrm{calc}} - E_{\mathrm{expt}}$, are observed for all 12 states considered in the table. This discrepancy is observed to grow with J and is systematically larger for H_3O^+ than for D_3O^+, behavior not seen in the smaller J states. In addition, within a given J manifold, $E_{\mathrm{calc}} - E_{\mathrm{expt}}$ appears to decrease with increasing K.

Table 4 also provides the energies obtained using the constants from the rigid rotor fit of the $J \leq 2$ DMC data. We first note that, although the DMC energies are not exclusively high relative to $E_{\mathrm{fit}}(J,K)$, the magnitude of $E_{\mathrm{calc}} - E_{\mathrm{fit}}$ mirrors the behavior seen above in $E_{\mathrm{calc}} - E_{\mathrm{expt}}$; $|E_{\mathrm{calc}} - E_{\mathrm{fit}}|$ grows with J and tends to be larger for the $|J,0,0\rangle$ states than for the $|J,J,0\rangle_{\pm}$ states. However, because the uncertainty in the fit generates large error bars at high J, statistically significant nonzero values of $E_{\mathrm{calc}} - E_{\mathrm{fit}}$ are only observed for the $|10,0,0\rangle$ state of both species as well as the $|6,0,0\rangle$ state of H_3O^+. Including all of the DMC data in the rigid rotor fit is found to yield an $E_{\mathrm{fit}}(J,K)$ that is much better able to replicate the $J = 10$ energies. However, this improved fit also gives energies for the $|6,0,0\rangle$ state of both species that are in poor agreement with the DMC data. Collectively, these observations suggest a significant difference in either the physics or the quality of our model's description of these systems at low and high values of J. We will return to the possible sources of this deviation in the following section.

3.2. Analysis of the Fixed-Node Treatment. In generating the excited states, we assumed that the nodal surfaces in the rotational wave functions are well captured by the zeros of the corresponding tesseral harmonics. One way to test this assumption is by comparing the energies obtained from calculations performed in different nodal regions of an excited state. If the nodes are properly placed, then these energies must be equal, within the statistical fluctuations of the simulations. For the $J = 1$ and $J = 2$ states, this condition is satisfied for both H_3O^+ and D_3O^+; i.e., for each of these states, there is no statistically significant difference between the average energies of the nodal regions at the 1% level. We have also investigated the energies in the different nodal regions for the $J = 6$ and $J = 10$ states considered in this study. Representative results are plotted in Figure 1.

For the $|10,10,0\rangle_-$ state of H_3O^+, the energies exhibit random fluctuations about the overall average energy of the state and their error bars overlap. The random nature of the fluctuations seen in Figure 1a suggests that they reflect statistical properties of the simulation rather than a manifestation of a problem with the choice of nodal surfaces. Note that the behavior of this state is very representative of the behavior seen in all of the high J, $|K| = J$ states considered in this study.

The situation is not as favorable for the $|10,0,0\rangle$ state of H_3O^+, as can be seen in Figure 1b. While the plot shows the expected symmetry, there is a $\sim$32 cm^{-1} gap between the average energies in the nodal regions adjacent to $\theta = 0$ and $\theta = \pi$ and those of the 9 middle regions. Within both groups of nodal regions, the average energies are in excellent agreement with each other. The same overall pattern is observed in the $|10,0,0\rangle$ state of D_3O^+, with a gap of $\sim$15 cm^{-1}, as well as in the $|6,0,0\rangle$ state of both species, where the differences are $\sim$11 cm^{-1} for H_3O^+ and $\sim$4 cm^{-1} for D_3O^+.

These observations suggest that the nodal surfaces used in our fixed-node DMC simulations of the high J, $K = 0$ states are not optimal and these deviations likely reflect couplings between K levels that decrease with increasing K. To get a sense of both the size and nature of this problem, we focus on the $|10,0,0\rangle$ state and consider how much we need to shift the position of the node near $\theta = 13.12°$ to bring the energies of the first two nodal regions into agreement. The results of this analysis for H_3O^+ are plotted in Figure 2. As shown in the figure, we can indeed achieve agreement between the average energies in these two nodal regions by shifting the location of the node toward a smaller value of θ. Moreover, the required shift is found to be quite small, only about 0.09°, indicating that the roots of $T_J^0(\theta,\chi)$ provide a reasonable set of locations for the nodes. Further, while the energies in the two nodal regions have

TABLE 2: Comparison between DMC, Experimental,[32,33] and Rigid Rotor Fit Energies (cm^{-1}) for States of H_3O^+ and D_3O^+ with $J = 1$ to $J = 2$

	H_3O^+			D_3O^+		
state	E_{calc}[a,b]	$E_{\mathrm{calc}} - E_{\mathrm{expt}}$[c]	$E_{\mathrm{calc}} - E_{\mathrm{fit}}$[d,e]	E_{calc}[a,b]	$E_{\mathrm{calc}} - E_{\mathrm{expt}}$[c]	$E_{\mathrm{calc}} - E_{\mathrm{fit}}$[d,e]
$\|1,1,0\rangle_+$	16.75 ± 3.27	−0.63 ± 3.27	−0.75 ± 2.96	9.13 ± 2.42	0.31 ± 2.42	−0.17 ± 1.89
$\|1,1,0\rangle_-$	17.61 ± 2.78	0.23 ± 2.78	0.11 ± 2.41	9.36 ± 2.80	0.54 ± 2.80	0.05 ± 2.35
$\|1,0,0\rangle$	23.12 ± 2.60	0.62 ± 2.60	0.23 ± 2.23	11.98 ± 2.21	0.63 ± 2.21	0.19 ± 1.62
$\|2,2,0\rangle_+$	48.05 ± 2.35	1.03 ± 2.35	0.40 ± 2.63	25.63 ± 2.08	1.69 ± 2.08	0.30 ± 1.73
$\|2,2,0\rangle_-$	47.62 ± 2.37	0.60 ± 2.37	−0.03 ± 2.65	24.96 ± 2.02	1.02 ± 2.02	−0.37 ± 1.66
$\|2,1,0\rangle_+$	63.20 ± 2.53	0.83 ± 2.53	−0.63 ± 2.66	32.90 ± 1.93	1.38 ± 1.93	0.10 ± 1.48
$\|2,1,0\rangle_-$	63.61 ± 2.37	1.24 ± 2.37	−0.22 ± 2.51	33.08 ± 2.21	1.56 ± 2.21	0.28 ± 1.84
$\|2,0,0\rangle$	69.83 ± 3.05	2.36 ± 3.05	0.61 ± 3.32	34.95 ± 2.13	0.91 ± 2.13	−0.34 ± 1.82

[a] DMC energies reported relative to ground state values given in Table 1. [b] Reported error bars are combined 99% confidence intervals of ground and rotationally excited states. [c] DMC energies relative to experiment [d] Rigid rotor fit based on calculated $J = 0$ to $J = 2$ DMC energies. [e] Reported error bars are combined 99% confidence intervals of DMC data and rigid rotor fit.

TABLE 3: Parameters from Rigid Rotor Fits of the DMC Data[a]

	H_3O^+		D_3O^+	
fit parameter	$J = 0$ to $J = 2$	all states	$J = 0$ to $J = 2$	all states
E_0	7452.23 ± 1.31	7448.56 ± 4.45	5474.67 ± 0.71	5473.60 ± 1.94
B	11.58 ± 0.33	12.46 ± 0.13	5.87 ± 0.18	6.19 ± 0.06
C	6.19 ± 0.44	6.30 ± 0.10	3.38 ± 0.24	3.18 ± 0.04

[a] Average values of B and C from the DMC ground state are 10.975 ± 0.015 and 6.116 ± 0.004 cm^{-1} for H_3O^+ and 5.587 ± 0.006 and 3.100 ± 0.001 cm^{-1} for D_3O^+. DMC data fit to functional form given by eq 13. Fit parameters are reported in cm^{-1} and error bars are 99% confidence intervals.

TABLE 4: Comparison between DMC, Experimental,[32,33] and Rigid Rotor Fit Energies (cm^{-1}) for States of H_3O^+ and D_3O^+ with $J = 6$ and $J = 10$

	H_3O^+			D_3O^+		
state	E_{calc}[a,b]	$E_{calc} - E_{expt}$[c]	$E_{calc} - E_{fit}$[d,e]	E_{calc}[a,b]	$E_{calc} - E_{expt}$[c]	$E_{calc} - E_{fit}$[d,e]
$\|6,6,0\rangle_+$	295.70 ± 2.13	7.39 ± 2.13	3.68 ± 16.16	150.09 ± 1.82	2.78 ± 1.82	− 7.02 ± 8.83
$\|6,6,0\rangle_-$	295.26 ± 2.08	6.95 ± 2.08	3.23 ± 16.15	149.79 ± 1.82	2.48 ± 1.82	− 7.32 ± 8.83
$\|6,0,0\rangle$	506.71 ± 3.34	36.36 ± 3.34	20.53 ± 14.20	253.61 ± 2.16	15.76 ± 2.16	6.86 ± 7.73
$\|10,10,0\rangle_+$	752.09 ± 2.06	25.35 ± 2.06	17.64 ± 44.49	378.68 ± 1.79	7.59 ± 1.79	− 18.49 ± 24.29
$\|10,10,0\rangle_-$	751.35 ± 2.08	24.61 ± 2.08	16.90 ± 44.49	379.22 ± 1.77	8.12 ± 1.77	− 17.95 ± 24.29
$\|10,0,0\rangle$	1371.22 ± 5.12	149.12 ± 5.12	97.46 ± 36.68	682.64 ± 2.87	61.84 ± 2.87	36.48 ± 19.99

[a] DMC energies reported relative to ground state values given in Table 1. [b] Reported error bars are combined 99% confidence intervals of ground and rotationally excited states. [c] DMC energies relative to experiment. [d] Rigid rotor fit based on calculated $J = 0$ to $J = 2$ DMC energies. [e] Reported error bars are combined 99% confidence intervals of DMC data and rigid rotor fit.

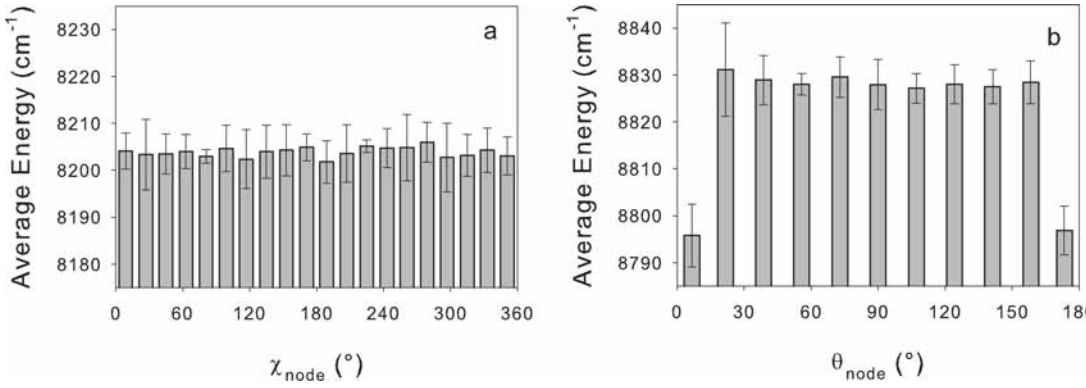

Figure 1. Average energy in each of the nodal regions of (a) the $|10,10,0\rangle_-$ and (b) the $|10,0,0\rangle$ states of H_3O^+. The error bars represent 99% confidence intervals.

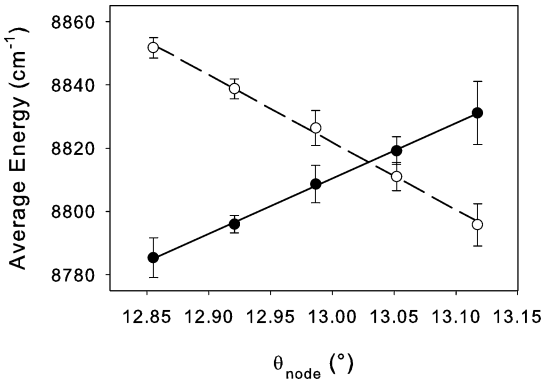

Figure 2. Average energy of the nodal regions of the $|10,0,0\rangle$ state of H_3O^+ bound to the left by $\theta = 0°$ (black circles) or $\theta = \theta°_{node}$ (white circles) for different values of θ_{node}. Error bars represent 99% confidence intervals and the lines are least-squares fits of the DMC data.

changed by ~17.7 cm^{-1}, their average value only increased by ~2.1 cm^{-1}. Similar analysis of the $|10,0,0\rangle$ state of D_3O^+ yielded a nearly identical shift in the nodal position, a shift in the energies by ~8.7 cm^{-1}, and an increase in the average energy by ~0.5 cm^{-1}.

3.3. Analysis of the Rotational Wave Functions. In an effort to further evaluate the results of our DMC calculations, we consider the projections of the overall molecular wave function and probability amplitude onto the rotational coordinates θ and χ. We first project the probability amplitude, obtained from the DMC simulations, onto θ or χ using the descendent weighting approach, described above. Comparison of these projections to the corresponding analytic functions provides a way to investigate how well the DMC probability amplitudes are represented by the tesseral harmonics. This comparison is made in Figure 3 for the $|2,1,0\rangle_+$ state of H_3O^+, where the agreement between the two distributions is shown to be quite poor. To understand this behavior, which is present in all of the states considered in this study, we use the distributions of walkers from the DMC simulations, without any descendent weighting, to project the magnitude of the wave function onto θ and χ. Comparing these to the analogous $|\Theta_{J,K}(\theta)|\sin(\theta)$ and $|X_{K_\pm}(\chi)|$ functions, we find that the agreement is now excellent, as evident in the congruence of the solid orange and black dashed lines of Figure 3. This breakdown of the descendent weighting approach for generating projections of $|\Psi|^2$ from instantaneous distributions of walkers reflects the fact that, aside from the infinite potential barriers placed along the nodal surfaces, the potential energy has no dependence on the rotational coordinates. As a result, the number of descendants

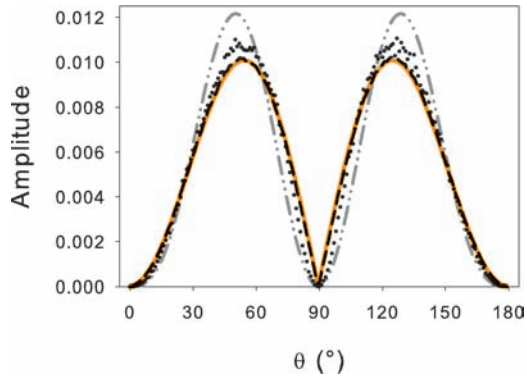

Figure 3. Comparison of the projection of the DMC probability amplitude onto θ (black dotted line) and the corresponding analytic expression, $|\Theta_{J,K}(\theta)|^2\sin(\theta)$ (gray dash-dot-dot line) for the $|2,1,0\rangle_+$ state of H_3O^+. These are contrasted with the projection of the DMC wave function onto θ (black dashed line) as well as $|\Theta_{2,1}(\theta)|\sin(\theta)$ (orange solid line).

that a given walker produces in N_{step} time steps is independent of the values of its rotational coordinates, preventing the w_i of eq 6 from providing a second effective copy of the wave function. Finally, as we have not imposed any assumptions on the shape of the wave function inside a nodal region, the good agreement between the DMC results and the tesseral harmonics is encouraging.

The comparison of the projections of the DMC wave functions onto θ or χ with the corresponding $|\Theta_{J,K}(\theta)|\sin(\theta)$ and $|X_{K_\pm}(\chi)|$ are also found to reflect the degree of convergence of the DMC calculations. For both species, the agreement between the DMC projections and the corresponding analytic histograms tends to improve as the number of nodal regions in a particular coordinate increases. This can be rationalized by noting that the size of the nodal regions tends to shrink as J or K increases and, as a result, the ensemble of walkers is required to sample a smaller fraction of the configuration space of the molecule. Numerically, this leads to more rapid convergence of the projections of the distribution of walkers along the θ and χ coordinates. On the basis of the differences in mass, this is found to be more pronounced for D_3O^+ than for H_3O^+. As shown in Figure 4, improving the equilibration of the DMC simulations of D_3O^+, either by increasing the length of the equilibration period or by starting with a larger and more homogeneous distribution of walkers, improves the agreement between the calculated projections and the analytic functions. We find that the improved equilibration also brought the average energies of these states into better agreement with the RVIB4 energies obtained by Bowman and co-workers.[24] In fact, we find that the differences between projections of the DMC wave function onto θ and χ and the corresponding $|\Theta_{J,K}(\theta)|\sin(\theta)$ and $|X_{K_\pm}(\chi)|$ functions provide a more sensitive measure of the degree of equilibration of the simulation than we are able to obtain by monitoring the average energy.

3.4. Vibrational Wave Functions. We now consider the extent to which rotational excitation changes the geometry of H_3O^+ and D_3O^+, beginning with their average bond lengths, $\langle r_{OH}\rangle$ and $\langle r_{OD}\rangle$, and average bond angles, $\langle \theta_{HOH}\rangle$ and $\langle \theta_{DOD}\rangle$. It is worth noting that the DMC method naturally captures the zero-point vibrational motion of the system so that all geometric quantities considered here and below represent averages over the ground vibrational state. As shown in Table 5, rotational excitation does indeed cause both quantities to increase via centrifugal forces. However, the changes are found to be well within the error bars for the $J = 1$ and $J = 2$ states of both species and quite subtle even for the $J = 10$ states. Indeed, the maximum observed increases of the average bond length and bond angle are only 0.0024 Å and 0.33°, respectively. Finally, we see in Table 5 that our method is able to capture the greater fluxionality of H_3O^+ relative to D_3O^+; the increase in $\langle r_{OH}\rangle$ and $\langle \theta_{HOH}\rangle$ caused by rotational excitation is observed to be roughly twice that of $\langle r_{OD}\rangle$ and $\langle \theta_{DOD}\rangle$.

The most significant geometrical change brought about by rotational excitation is captured by the planarity distance, Γ, a coordinate defined to be the distance of the oxygen atom from the plane defined by the three hydrogen or deuterium atoms. This internal coordinate tracks the umbrella motion of the molecule, achieving a value of 0 when the molecule assumes a planar geometry. Projections of the overall molecular wave functions of H_3O^+ and D_3O^+ onto this coordinate are shown in Figure 5 for the $|0,0,0\rangle$, $|10,0,0\rangle$, and $|10,10,0\rangle_+$ states. A clear increase in probability amplitude around $\Gamma = 0$ with rotational excitation is evident in both panels, although as with the other geometric quantities, the effect is much more pronounced for H_3O^+ than for D_3O^+. Moreover, we see that the Γ distribution for the $|10,10,0\rangle_+$ state displays a much larger deviation from the ground state distribution than that of the $|10,0,0\rangle$ state.

Combining the effects of rotational excitation on the bond lengths, bond angles, and planarity distances in H_3O^+ and D_3O^+ illustrates the ability of our method to probe the effects of centrifugal distortion on the structure of highly fluxional molecules. When $|K| = J$, that is, when the molecule's rotational motion is nearly completely about its symmetry axis, the centrifugal forces push the molecule into a more planar average structure. As demonstrated by the results in Table 5, this shift toward planarity is accompanied by a shift toward larger bond angles. The average bond lengths of the $|J,J,0\rangle_\pm$ states are also increased, but it appears that for this type of rotational motion, the centrifugal distortion primarily affects the molecule's shape rather than its size. In contrast, when $K = 0$ and the rotational motion is entirely about some axis perpendicular to the symmetry axis, the largest geometric change occurs in the bond lengths; the bond length increase in the $|10,0,0\rangle$ state is over twice that for the $|10,10,0\rangle_\pm$ states. Likewise, the changes in the Γ distribution, as well as the increase in the average bond angles, are much less pronounced for the states with $K = 0$.

4. Discussion

While, overall, the rotational DMC approach seems to be working quite well, and the agreement with the $J = 1$ energies obtained by a converged variational calculation using the same potential surface is excellent, the deviations from the rigid rotor model at high J are of some concern. It is further surprising that the energies that are calculated for these states are larger than those obtained from a rigid rotor fit of the DMC energies with $J \leq 2$. In general, one expects that centrifugal distortion and rotation−vibration interactions will both cause the energy to be lower than the rigid rotor energies. This lowering should increase with J. This is exactly opposite of the behavior of the energies that have been obtained in the present study. There are several possible sources for this behavior.

The first is that this is a fundamental property of H_3O^+ and is a reflection of large rotation−vibration interactions brought about by the large amplitude motions along the tunneling coordinate. One way to investigate this possibility is to see if the energies obtained using the model Hamiltonians that were used to fit the experimentally observed transition frequencies[32,33] show the same J dependence as those obtained from our DMC simulations. As shown in Tables 2 and 4, the trends in $|E_{calc} -$

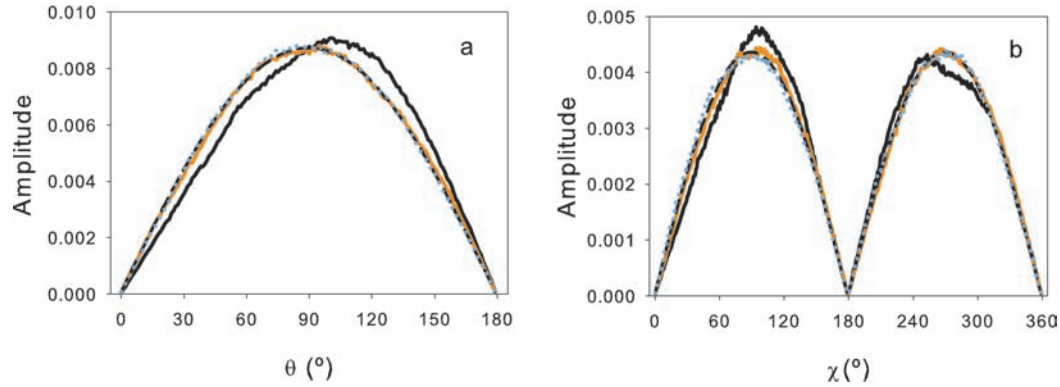

Figure 4. Sensitivity of the DMC wave functions to equilibration is investigated by comparing (a) $|\Theta_{0,0}(\theta)|\sin(\theta)$ (orange solid line), to the projection of the $|0,0,0\rangle$ DMC wave functions onto θ for H_3O^+ (blue dotted line), D_3O^+ obtained with 20 000 equilibration time steps (black solid line), and D_3O^+ obtained with 30 000 equilibration time steps (black dashed line). Similarly, in (b) we plot $|X_{1_+}(\chi)|$ (orange solid line) and compare it to the projection of the $|1,1,0\rangle_+$ DMC wave functions onto χ for H_3O^+ (blue dotted line), D_3O^+ with 20 000 D_3O^+ walkers used in ground state equilibration (black solid line), and D_3O^+ with 80 000 H_3O^+ walkers used in ground state equilibration (black dashed line).

TABLE 5: Average Bond Lengths and Bond Angles of the $J = 0$ and $J = 10$ States of H_3O^+ and D_3O^+ [a]

	H_3O^+		D_3O^+	
state	$\langle r_{OH}\rangle$ (Å)	$\langle \theta_{HOH}\rangle$ (deg)	$\langle r_{OD}\rangle$ (Å)	$\langle \theta_{DOD}\rangle$ (deg)
$\|0,0,0\rangle_+$	0.99536 ± 0.00026	113.062 ± 0.041	0.99070 ± 0.00020	112.584 ± 0.031
$\|10,10,0\rangle_+$	0.00107 ± 0.00027	0.334 ± 0.043	0.00053 ± 0.00021	0.166 ± 0.032
$\|10,10,0\rangle_-$	0.00103 ± 0.00027	0.334 ± 0.043	0.00057 ± 0.00021	0.173 ± 0.032
$\|10,0,0\rangle$	0.00236 ± 0.00029	0.218 ± 0.045	0.00126 ± 0.00022	0.115 ± 0.034

[a] Reported error bars are 99% confidence intervals. Geometric parameters of $J = 10$ states reported relative to ground state.

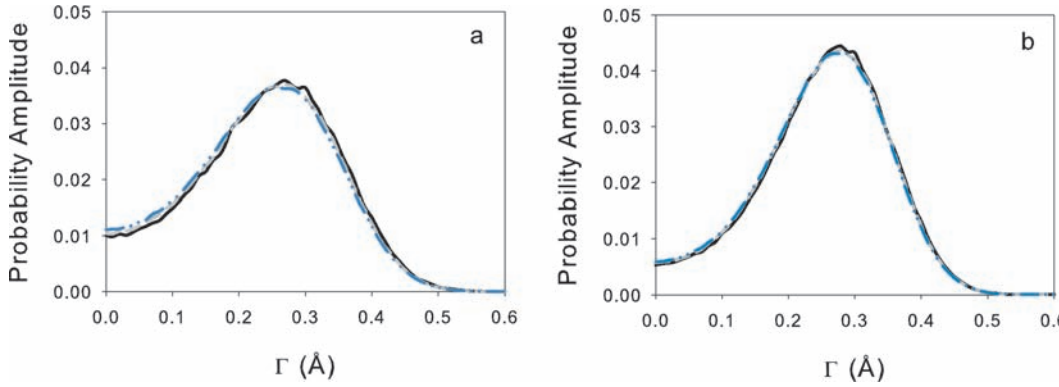

Figure 5. Plots of the projections of the DMC probability amplitude onto Γ for (a) H_3O^+ and (b) D_3O^+. Results for the $|0,0,0\rangle$ (black solid line), $|10,0,0\rangle$ (gray dashed line), and $|10,10,0\rangle_+$ (blue dash-dot-dot line) states are reported.

$E_{expt}|$ mirror those for $|E_{calc} - E_{fit}|$, with both quantities achieving their largest values for the $K = 0$ levels with large J. While the experimental data sets contain transitions involving many of the states considered in this study, few transitions involving $|J,0,0\rangle$ states have been assigned and it is not clear how well the energies of these states are reproduced by the experimental constants. Based on the above discussion, we do not believe that the calculated behavior is a fundamental property of H_3O^+ and D_3O^+, at least not to the magnitude predicted by our simulations.

A second possibility arises from the fact that rotation−vibration mixing may lead to more complex nodal structures than can be captured in our model. For example, there is a coupling between the states with $K = 0$ and no node in the inversion coordinate and states with $|K| = 3$ and a node in the inversion coordinate. These states are expected to be close in energy, although analysis of the experimental parameters indicates that inclusion of this term shifts the energy by <1 cm^{-1}. A second manifestation of rotation−vibration mixing comes in the fact that while the model Hamiltonian has a simple form where the energies can be expressed as polynomials in J and K, this Hamiltonian results from applying perturbation theory to the full rotation/vibration Hamiltonian.[4] In doing this, the wave functions that make up the basis in this dressed representation also have been perturbatively corrected and are no longer simple products of rotational and vibrational contributions. As such the *true* nodal surfaces may not be as simple as the model suggests.

Finally, in our studies of vibrationally excited states, we have found that for states with $v = 0$ or 1, the fixed-node approximation works quite well,[18,23] although it is expected to break down for higher values of v. Likewise one could anticipate that the description of the nodal surfaces for the rotational motions could break down with increasing J. Even the $J = 6$ calculations have more nodal regions than any fixed-node vibrational calculations preformed in our group, or by others.

In the absence of more accurate calculations of rotational energies at higher values of J, it is hard to determine exactly where the source of the discrepancy arises from. We cannot definitively attribute the behavior to the model used in the calculations or to unexpected behavior of the rotational energy

levels in H_3O^+. It would be interesting to have additional information about these states, either from experiment or from calculations.

5. Conclusion

In this paper, we presented an approach for obtaining energies and wave functions of rotationally excited states using diffusion Monte Carlo simulations. By all measures, the approach works very well for $J \leq 2$. For higher values of J, larger deviations are found between the calculated energies and those obtained from either the experimental fits or our rigid rotor fits of the $J \leq 2$ DMC data. We believe these differences to be the result of the incomplete treatment of rotation−vibration interactions by our approach, although we do not fully dismiss the possibility that the unexpected behavior is a result of the large amplitude motion exhibited by H_3O^+ and D_3O^+, even in their ground vibrational states.

While it is good to see that such an approach is effective for studies of a tetratomic molecule, like H_3O^+, its power will be in analyzing rotation−vibration interactions in larger fluxional molecules, in particular CH_5^+. In addition, the theory, to date, is limited to symmetric top molecules, for which the functional form of the rotational wave functions does not depend strongly on the molecular geometry. This will not necessarily be the case for most molecules, including partially deuterated H_3O^+ or CH_5^+, which are asymmetric tops. An additional area of investigation is the coupling of these rotational studies with previously proposed surface hopping techniques to allow us to investigate molecules that are asymmetric rotors.[34]

Acknowledgment. Support through grant CHE-0515627 from the Chemistry Division of the National Science Foundation is gratefully acknowledged. We also thank Professor Joel M. Bowman for providing us with the codes used to evaluate the potential used in this work. This work was supported in part by an allocation of computing resources from the Ohio Supercomputer Center.

References and Notes

(1) Keske, J.; McWhorter, D. A.; Pate, B. H. *Int. Rev. Phys. Chem.* **2000**, *19*, 363–407.
(2) Hougen, J. T.; Kleiner, I.; Godefroid, M. *J. Mol. Spectrosc.* **1994**, *163*, 559–86.
(3) Just, G. M. P.; McCoy, A. B.; Miller, T. A. *J. Chem. Phys.* **2007**, *127*, 044310/1−11.
(4) van Vleck, J. H. *Phys. Rev.* **1935**, *47*, 487–94.
(5) McCoy, A. B.; Burleigh, D. C.; Sibert, E. L. *J. Chem. Phys.* **1991**, *95*, 7449–65.
(6) Ernesti, A.; Hutson, J. M. *Chem. Phys. Lett.* **1994**, *222*, 257–62.
(7) Sandler, P.; Buch, V.; Sadlej, J. *J. Chem. Phys.* **1996**, *105*, 10387–97.
(8) Lee, H.-S.; McCoy, A. B. *J. Chem. Phys.* **2001**, *114*, 10278–87.
(9) Eckart, C. *Phys. Rev.* **1935**, *47*, 552–8.
(10) Louck, J. D.; Galbraith, H. W. *Rev. Mod. Phys.* **1976**, *48*, 69–106.
(11) Wilson, E. B.; Decius, J. C.; Cross, P. C. *Molecular Vibrations*; Dover: New York, 1955.
(12) Frederick, J. H.; McClelland, G. M.; Brumer, P. *J. Chem. Phys.* **1985**, *83*, 190–207.
(13) Anderson, J. B. *J. Chem. Phys.* **1975**, *63*, 1499–1503.
(14) Anderson, J. B. *J. Chem. Phys.* **1976**, *65*, 4121–27.
(15) Suhm, M. A.; Watts, R. O. *Phys. Rep.* **1991**, *204*, 293–329.
(16) Kuhn, B.; Rizzo, T. R.; Luckhaus, D.; Quack, M.; Suhm, M. A. *J. Chem. Phys.* **1999**, *111*, 2565–2587.
(17) Brown, A.; McCoy, A. B.; Braams, B. J.; Jin, Z.; Bowman, J. M. *J. Chem. Phys.* **2004**, *121*, 4105–4116.
(18) McCoy, A. B.; Huang, X.; Carter, S.; Bowman, J. M. *J. Chem. Phys.* **2005**, *123*, 064317.
(19) Cho, H. M.; Singer, S. J. *J. Phys. Chem. A* **2004**, *108*, 8691–8702.
(20) Blume, D.; Lewerenz, M.; Whaley, K. B. *J. Chem. Phys.* **1997**, *107*, 9067–78.
(21) Moroni, S.; Blinov, N.; Roy, P.-N. *J. Chem. Phys.* **2004**, *121*, 3577–3581.
(22) Ceperley, D. M.; Bernu, B. *J. Chem. Phys.* **1988**, *89*, 6316–28.
(23) Lee, H.-S.; McCoy, A. B. *J. Chem. Phys.* **2002**, *116*, 9677–89.
(24) Huang, X.; Carter, S.; Bowman, J. M. *J. Chem. Phys.* **2003**, *118*, 5431.
(25) Rajamäki, T.; Miani, A.; Halonen, L. *J. Chem. Phys.* **2003**, *118*, 10929–10938.
(26) McCoy, A. B. *Int. Rev. Phys. Chem.* **2006**, *25*, 77–108.
(27) McCoy, A. B. In *Recent Advances in Quantum Monte Carlo Methods*; Anderson, J. B., Rothstein, S. M., Eds.; ACS Symposium Series 953; 2006; Vol. 3, pp 147−64.
(28) Feit, M. D.; Fleck, J. A. *J. Chem. Phys.* **1983**, *78*, 301–308.
(29) Anderson, J. B. *Int. Rev. Phys. Chem.* **1995**, *14*, 85–112.
(30) Hinkle, C. E.; McCoy, A. B. *J. Phys. Chem A* **2009**, *113*, 4587–97.
(31) Zare, R. N. *Angular Momentum: Understanding Spatial Aspects in Chemistry and Physics*; Wiley Interscience: New York, 1988.
(32) Tang, J.; Oka, T. *J. Mol. Spectrosc.* **1999**, *196*, 120–130.
(33) Araki, M.; Ozeki, H.; Saito, S. *Mol. Phys.* **1999**, *97*, 177–183.
(34) McCoy, A. B. *Chem. Phys. Lett.* **2000**, *321*, 71–77.

JP905098K